

Development, Verification and Validation of Enclosure Radiation Capabilities in the CHarring Ablator Response (CHAR) Code

Giovanni Salazar*, Justin C. Droba†, Brandon Oliver‡ and Adam J. Amar§

NASA Lyndon B. Johnson Space Center, Houston, TX, 77058, USA

With the recent development of multi-dimensional thermal protection system (TPS) material response codes including the capabilities to account for radiative heating is a requirement. This paper presents the recent efforts to implement such capabilities in the CHarring Ablator Response (*CHAR*) code developed at NASA's Johnson Space Center. This work also describes the different numerical methods implemented in the code to compute view factors for radiation problems involving multiple surfaces. Furthermore, verification and validation of the code's radiation capabilities are demonstrated by comparing solutions to analytical results, to other codes, and to radiant test data.

The work presented in this paper will be closely related to an ITAR session paper on using these enclosure radiation capabilities to reduce Orion Flight Data. However, since the implementation and verification/validation are not ITAR, it was decided to publish this in one of the open sessions.

* Aerospace Engineer, Aeroscience and CFD Branch, AIAA Member.

† Aerospace Engineer, Aeroscience and CFD Branch, AIAA Member.

‡ Aerospace Engineer, Aeroscience and CFD Branch, AIAA Member.

§ Aerospace Engineer, Aeroscience and CFD Branch, AIAA Member.

I. Introduction

During re-entry, a spacecraft's thermal protection system (TPS) is exposed to different modes of heat transfer such as convection, conduction and radiation. When considering simple planar geometries and low entry velocities, radiation heating can be neglected due to its low relative magnitude when compared to convection and conduction. However, missions involving lunar-type re-entry velocities must account for significant shock layer radiation. Also, when considering more complicated geometries on a vehicle which result in partial or total enclosures, the radiation of thermal energy between the different parts of the enclosure must be accounted for. Enclosures such as those resulting on a vehicle's TPS from micrometeoroid and orbital debris (MMOD) impact are of particular importance to vehicle designers.

With the recent development of multi-dimensional thermal material response codes, including the capabilities to account for radiative heating is essentially a requirement. This paper presents the recent efforts to implement such capabilities in the CHarring Ablator Response (CHAR) code developed at NASA's Johnson Space Center. This work also describes the different numerical methods implemented in the code to compute view factors for radiation problems involving multiple surfaces. Furthermore, verification and validation of the code's radiation capabilities are demonstrated by comparing solutions to analytical results, to other codes, and to radiant test data.

II. Numerical Method

The radiation capabilities described in this work are implemented within the *CHAR* framework. *CHAR* is a 1D/2D/3D material thermal response code which solves general heat transfer problems on decomposing charring ablators as well as non-decomposing, non-charring TPS materials, in serial or parallel. The general governing equations being solved in *CHAR* are briefly outlined in this section for completeness; however, a more complete description can be found in (Reference which will be published in this conference as well providing an Overview of CHAR).

The equations that govern the solid/gas system of the porous charring ablator include energy and mass conservation equations for the solid as well as the Navier-Stokes equations as applied to all of the gaseous species considered. In the general case, it is possible that the pyrolysis gases react with the remaining solid, or deposit residue (coke) on the solid, but these phenomena are neglected. Under the assumptions that the pyrolysis gas is in thermochemical equilibrium and the solid and gas are in thermal equilibrium, the solid energy equation on a moving mesh reduces to a nodal mixture energy equation given by

$$\left. \frac{\partial(\rho e_o)}{\partial t} \right|_{node} = \nabla \cdot (\mathbf{k} \nabla T) - \nabla \cdot (\phi \rho_g h_{o_g} \mathbf{v}_g) + \dot{Q} + \mathbf{v}_m \cdot \nabla(\rho e_o) \quad (1)$$

where ρ , e_o , ϕ , h_o , \mathbf{v} , and \dot{Q} denote density, total energy, porosity, total enthalpy, velocity, and volumetric energy source, respectively, and the subscript g denotes a quantity with respect to the pyrolysis gases. And \mathbf{v}_m denotes the

mesh velocity at a node. Since ablators in general can be anisotropic materials, the thermal conductivity, \mathbf{k} , is a second order tensor.

If it is assumed that all solid decomposition results in pyrolysis gas generation, the gases are free to flow through the porous medium, and the gases occupy all of the pore space, then the nodal gas mass conservation equation, including mesh convection terms, is given by

$$\left. \frac{\partial(\phi\rho_g)}{\partial t} \right|_{node} = \dot{\omega}_g - \nabla \cdot (\phi\rho_g \mathbf{v}_g) + \mathbf{v}_m \cdot \nabla(\phi\rho_g) \quad (2)$$

where the porous flow gas velocity is given by a porous flow law such as Darcy's law:

$$\mathbf{v}_g = \frac{Q}{\phi A} = -\frac{\kappa}{\phi\mu} \nabla P \quad (3)$$

Transient momentum equations have been included as a modeling option in *CHAR*; however, only Darcy's law is presented in this document for the sake of brevity.

The solid mass conservation equation is solved on a stationary mesh, and is simply

$$\left. \frac{\partial\rho_s}{\partial t} \right|_{\mathbf{x}} = \dot{\omega}_s \quad (4)$$

CHAR discretizes the governing equations according to the Galerkin finite element method. Multiplying the energy equation, Eqn. (1), by a suitable test function, v , and integrating over the domain Ω while integrating the second and third terms by parts to give the natural boundary condition terms, the weak statement becomes: Find $\rho_{e_o} \in H^1$ such that

$$\int_{\Omega} \left[v \frac{\partial(\rho_{e_o})}{\partial t} + \nabla v \cdot (\mathbf{k} \nabla T) - \nabla v \cdot (\phi\rho_g h_{o_g} \mathbf{v}_g) - v \mathbf{v}_m \cdot \nabla(\rho_{e_o}) - v \dot{Q} \right] d\Omega + \oint_{\Gamma} (v h_{o_g} \dot{m}_g + v \dot{q}_{cond_s}) d\Gamma = 0 \quad \forall v \in H_0^1 \quad (5)$$

where the boundary mass flux due to gas convection is

$$\dot{m}_g = (\phi\rho_g) \mathbf{v}_g \cdot \hat{\mathbf{n}} \quad (6)$$

and the boundary heat flux is

$$\dot{q}_{cond_s} = -\mathbf{k} \nabla T \cdot \hat{\mathbf{n}} \quad (7)$$

Likewise, a Galerkin weak statement can be developed for the gas mass conservation equation, Eqn. (2): Find

$\phi\rho_g \in H^1$ such that

$$\int_{\Omega} \left(\frac{\partial(\phi\rho_g)}{\partial t} v - \nabla v \cdot (\phi\rho_g \mathbf{v}_g) - v \mathbf{v}_m \cdot \nabla(\phi\rho_g) + \dot{\omega}_s v \right) d\Omega + \oint_{\Gamma} v \dot{m}_g d\Gamma = 0 \quad \forall v \in H_0^1 \quad (8)$$

In *CHAR*, the system of equations is advanced in time according to first and second order implicit time integrators. The nonlinear set of governing equations are solved in parallel via Newton's method with exact complex-perturbation Jacobians, and several options are available via the PETSc library [1] to solve the implicit linear system.

There are many different boundary conditions available for the energy and gas equations in *CHAR* such as specified convective heating, specified heat flux, specified temperature, contact conduction, specified pressure, specified mass flux, thermochemical ablation using B' tables, specified ablation, CFD coupling, surface melting, etc. This work focuses on the code's enclosure radiation capabilities, which are described in further detail in the following sections.

A. Enclosure Radiation Boundary Condition

The net radiative heat flux from a face, \dot{q}_i , is the flux emitted by a diffuse surface, E_i , less the amount of the incident radiation, G_i , absorbed by the surface:

$$\dot{q}_i = E_i - \epsilon_i G_i \quad (9)$$

where

$$E_i = \sigma \epsilon_i T_i^4 \quad (10)$$

$$G_i = \sum_j F_{ij} J_j \quad (11)$$

and F_{ij} is the view factor from face i to face j . The amount of incident energy not absorbed is reflected if the surfaces are assumed to be opaque. Therefore, the resulting radiosity, J_i , from the surface is the combination of the emitted energy and the reflected energy.

$$J_i = E_i + \rho_i G_i \quad (12)$$

with a reflectance given by

$$\rho_i = 1 - \epsilon_i \quad (13)$$

Substituting the radiosity into the incident radiation term a few times yields:

$$\begin{aligned}
G_i &= \sum_j F_{ij} J_j \\
G_i &= \sum_j F_{ij} (E_j + \rho_j G_j) \\
G_i &= \sum_j F_{ij} E_j + \sum_j F_{ij} \rho_j \left(\sum_k F_{jk} J_k \right) \\
G_i &= \sum_j F_{ij} E_j + \sum_j F_{ij} \rho_j \sum_k F_{jk} (E_k + \rho_k G_k) \\
G_i &= \sum_j F_{ij} E_j + \sum_j F_{ij} \rho_j \sum_k F_{jk} E_k + \sum_j F_{ij} \rho_j \sum_k F_{jk} \rho_k \left(\sum_m F_{km} J_m \right) \\
G_i &= \sum_j F_{ij} E_j + \sum_j F_{ij} \rho_j \sum_k F_{jk} E_k + \sum_j F_{ij} \rho_j \sum_k F_{jk} \rho_k \sum_m F_{km} (E_m + \rho_m G_m)
\end{aligned}$$

$$\overbrace{G_i}^{\text{incident radiation}} = \overbrace{\sum_j F_{ij} E_j}^{\text{direct emission}} + \overbrace{\sum_j F_{ij} \rho_j \sum_k F_{jk} E_k}^{\text{first reflection}} + \overbrace{\sum_j F_{ij} \rho_j \sum_k F_{jk} \rho_k \sum_m F_{km} (E_m + \rho_m G_m)}^{\text{subsequent reflections}} \quad (14)$$

It would be desirable to develop an iterative method to compute the total incident radiation including reflections. This is done by sequentially evaluating terms in this expression (where the number of terms is the number of reflections a particular emitted photon is allowed to experience before being ignored). With a few observations of the expression, this is feasible. Notice that each term contains something similar to

$$G_{e,i}^0 = \sum_j F_{ij} E_j, \quad (15)$$

which represents the source of the energy in the radiation field. This can be evaluated without regard for any reflections. Substituting this in, the overall expression reduces to:

$$G_i = G_{e,i}^0 + \sum_j F_{ij} \rho_j G_{e,j}^0 + \sum_j F_{ij} \rho_j \sum_k F_{jk} \rho_k G_{e,k}^0 + \text{remainder}. \quad (16)$$

The amount of incident radiation from the first reflection is

$$R_i^0 = \sum_j F_{ij} \rho_j G_{e,j}^0 \quad (17)$$

and subsequent reflections are given by

$$R_i^n = \sum_j F_{ij} \rho_j R_j^{(n-1)}. \quad (18)$$

Substituting in for the overall incident radiation:

$$G_i = G_{e,i}^0 + R_i^0 + \sum_j F_{ij} \rho_j R_j^0 + \text{remainder} \quad (19)$$

$$G_i = G_{e,i}^0 + \sum_{n=1}^N R_i^n. \quad (20)$$

Because ρ is always less than 1, the values for R_i^n will converge to zero. From this, it is apparent that by making multiple passes through the communicating faces, the total incident radiation for a given number of reflections can be built up based on surface temperatures and the incident radiation from the previous reflection number, and that this value will converge as more reflections are taken into account. **An alternative approach to account for reflections is currently being implemented and will be presented in this section as well.**

Within *CHAR*, the enclosure radiation boundary condition is cast in the same form as a typical reradiation flux, given by

$$\dot{q}_{rerad} = \sigma \epsilon (T_w^4 - T_\infty^4) \quad (21)$$

where ϵ is the emissivity of the solid surface. However, to incorporate the effects of reradiating faces, T_∞ is replaced by T_{eq} , resulting in

$$\dot{q}_{rerad} = \sigma \epsilon (T_w^4 - T_{eq}^4) \quad (22)$$

The radiation exchange is computed from the temperature of the visible participating faces using the method described in this section. The specific value of T_{eq} can be computed in a number of ways, depending on how the view factors, F_{ij} , are computed. There are currently two methods supported for approximating this term.

To put Eqn. (20) in terms consistent with the reradiation boundary condition, the equivalent farfield temperature is computed to represent G_i according to

$$G_i = \sigma T_{eq}^4. \quad (23)$$

B. Computation of View Factors

The exact definition of the view factor from element face i to element face j is given by

$$F_{ij} = \frac{1}{A_i} \int_{A_i} \int_{A_j} \frac{\cos \theta_i \cos \theta_j}{\pi R^2} dA_j dA_i, \quad (24)$$

where the terms are defined in Figure (Add figure here) ???. With the exact view factors, the definition of T_{eq} is given by Eqn. (23).

The first and most accurate method to calculate the view factors is to numerically integrate Eqn. (24) by dividing participating element faces into K sub-faces, where K is a user input. The integrals can now be expressed as

summations.

$$F_{ij} = \frac{1}{A_i} \sum_{l=1}^K \sum_{m=1}^K \frac{\cos(\theta_i)_l \cos(\theta_j)_m}{\pi R_{l \rightarrow m}^2} (A_j)_m (A_i)_l \quad (25)$$

where the angles and areas are defined with respect to the sub-faces. The outer “ l ” summation is over sub-faces on element face i , and the inner “ m ” summation is over sub-faces on element face j . Consequently, the total areas of the element faces are given by

$$A_i = \sum_{l=1}^K (A_i)_l$$

and

$$A_j = \sum_{m=1}^K (A_j)_m$$

Prior to the assembly of the FEM matrix, the full matrix of view factors is computed. Only boundary faces that are specified as having enclosure radiation are currently considered to participate in radiation exchange. To account for the fact that two faces may not be able to see each other due to obstruction by other faces (referred to as shadowing), the user can optionally specify that a search be performed to verify that the $R_{l \rightarrow m}$ paths are not obstructed by any other face. If an obstruction is found, the view factor contribution from those sub-faces is set to 0. If two faces have normals that do not point toward each other, the view factor is set to 0. If the view factors for face i do not sum to 1.0, the difference is made up by a view factor to a ‘far-field’ face with temperature T_∞ . Note that this method does not account for partially shadowed faces since only the center-to-center R path is checked for obstructions.

The second method available to compute view factors involves a Monte Carlo ray-tracing algorithm. In this approach a large number of statistical experiments are carried out from any given face by randomly selecting the origin of a ray (or photon). By treating each face as a diffuse emitter, each ray emission direction is also randomly selected according to a cosine probability distribution. Once a total number of rays N are casted from an element face i , the view factor to any other face j is given by

$$F_{ij} = \frac{m}{N}$$

where m is the total number of rays emitted from face i which intersected face j .

This approach is especially powerful in dealing with complex geometries as it implicitly takes into account shadowing and partial shadowing. However, due to the non-deterministic nature of this approach, the analyst must ensure sufficient rays are being casted from each face to correctly resolve the view factors. It is also well known that the error in this Monte Carlo approach is inversely proportional to the square root of number of rays emitted (for a given element face size). Therefore, increasing the number of rays emitted will lead to better view factor convergence. To speed up the many ray-intersection and searches involved with this approach, an octree structure and an efficient octree traversal algorithm have been implemented in *CHAR*. Extensive work has been done to date to develop the octree algorithm and the intersection detection method. A lot of detail on that work will be added to this paper.

For both of these methods, the equivalent temperature, T_{eq} , is given by Eqn. (23) once all the view factors are known. The T_{eq} for each participating boundary face is computed at the beginning of each time step. Accepting the boundary condition to be explicit in T_{eq} permits the FEM implementation of this term to be identical to that of *CHAR*'s reradiation boundary condition.

III. Code Verification

A. Spherical Radiation Gap (Three-Dimensional)

1. Problem Statement

This problem is intended to determine the order of accuracy of the enclosure radiation model in *CHAR*. While this is not a true verification exercise because the theoretical order of accuracy for the view factor methodology is not known, it is a useful exercise to show that the correct answer is being approached as the grid is refined.

Consider two concentric spherical shells with a non-conducting radiation gap between them. The spheres are made of different opaque, gray, diffuse emitting and reflecting materials each with their own constant thermal conductivity, emissivity, and absorptivity. The outer surface of the outer shell and the inner surface of the inner shell are subject to constant temperature conditions T_o and T_i respectively. The only energy transfer mechanism between the two shells is radiation exchange, including emission, absorption, and reflection. A schematic outlining the problem geometry can be seen in Figure 1. Since the extreme outer and inner boundaries of the problem are subject to constant isothermal conditions, this problem will reach a one-dimensional steady state temperature profile, varying only in the radial direction. The parameters used in this problem are shown in Table 1.

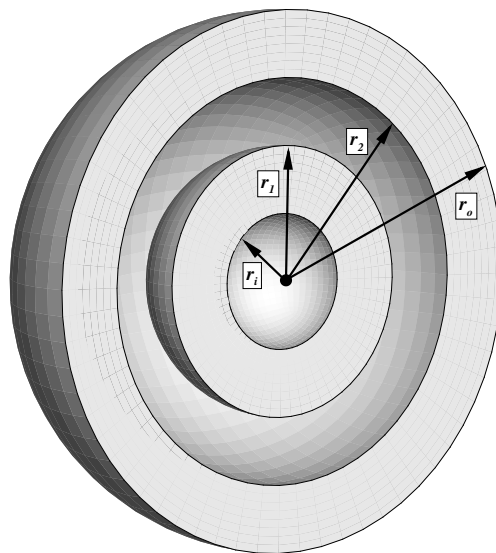


Figure 1. Concentric spherical shells geometry (cut in half).

Table 1. Spherical radiation gap problem parameters.

$$\begin{aligned}
 k_1 &= 2.0 \text{ W/m}\cdot\text{K} \\
 k_2 &= 0.35 \text{ W/m}\cdot\text{K} \\
 \epsilon_1 &= \alpha_1 = 0.5 \\
 \epsilon_2 &= \alpha_2 = 0.8 \\
 r_i &= 0.01 \text{ m} \\
 r_1 &= 0.02 \text{ m} \\
 r_2 &= 0.03 \text{ m} \\
 r_o &= 0.04 \text{ m} \\
 T_i &= 300 \text{ K} \\
 T_o &= 1300 \text{ K}
 \end{aligned}$$

2. Analytic Solution

Since a steady-state is reached, the functional form of the temperature distribution for each shell can be independently determined according to the analytic steady-state solution for a single spherical shell with isothermal boundary conditions. The equations that govern the steady-state response for a constant property spherical shell subject to isothermal conditions on the inner "i" and outer "o" faces are

$$\frac{1}{A} \frac{d}{dr} \left(kA \frac{dT}{dr} \right) = 0 \quad (26)$$

$$T(r_o) = T_o \quad (27)$$

$$T(r_i) = T_i \quad (28)$$

where the area, A , for the spherical geometry is $4\pi r^2$. The analytic solution is given by

$$T(r) = T_i + (T_o - T_i) \left(\frac{\frac{1}{r_i} - \frac{1}{r}}{\frac{1}{r_i} - \frac{1}{r_o}} \right) \quad (29)$$

The heat fluxes on the inner and outer surface are

$$\dot{q}_i = -k \frac{dT}{dr} \Big|_{r=r_i} = -k (T_o - T_i) \left(\frac{\frac{1}{r_i^2}}{\frac{1}{r_i} - \frac{1}{r_o}} \right) \quad (30)$$

$$\dot{q}_o = -k \frac{dT}{dr} \Big|_{r=r_o} = -k (T_o - T_i) \left(\frac{\frac{1}{r_o^2}}{\frac{1}{r_i} - \frac{1}{r_o}} \right) \quad (31)$$

The constant heating rate through the spherical shell can now be derived.

$$Q = \dot{q}_o A_o = \dot{q}_i A_i = 4\pi k (T_i - T_o) \left(\frac{r_i r_o}{r_o - r_i} \right) \quad (32)$$

Using the analytic solution to the single spherical shell problem in Eqn. (29), the temperature distributions in each of the inner and outer spherical shells for the radiation gap problem can be determined.

$$\left. \begin{aligned} \text{Inner Shell: } T(r) &= T_i + (T_1 - T_i) \left(\frac{\frac{1}{r_i} - \frac{1}{r}}{\frac{1}{r_i} - \frac{1}{r_1}} \right) \\ \text{Outer Shell: } T(r) &= T_2 + (T_o - T_2) \left(\frac{\frac{1}{r_2} - \frac{1}{r}}{\frac{1}{r_2} - \frac{1}{r_o}} \right) \end{aligned} \right\} \quad (33)$$

Where T_1 and T_2 are the temperatures at the outer surface of the inner shell, $r = r_1$, and the inner surface of the outer shell, $r = r_2$, respectively. These are the two surfaces participating in the radiation exchange between the shells. These temperatures can be determined by examining the energy balances on the radiating surfaces. Since a steady-state has been reached, the heat conducted through a given shell must equal the heat radiated into the shell. The energy balances on the radiating surfaces are

$$\left. \begin{aligned} \text{Inner Shell: } 4\pi k_1 \frac{r_1 r_i}{r_1 - r_i} (T_i - T_1) &= A_1 \mathcal{F}_{12} \sigma (T_1^4 - T_2^4) \\ \text{Outer Shell: } 4\pi k_2 \frac{r_2 r_o}{r_o - r_2} (T_2 - T_o) &= A_1 \mathcal{F}_{12} \sigma (T_1^4 - T_2^4) \end{aligned} \right\} \quad (34)$$

where the exchange factor for two concentric diffuse-gray spheres is given by

$$A_1 \mathcal{F}_{12} = A_2 \mathcal{F}_{21} = \left(\frac{\rho_1}{\epsilon_1 A_1} + \frac{1}{A_1} + \frac{\rho_2}{\epsilon_2 A_2} \right)^{-1} \quad (35)$$

where the reflectance, ρ , is given by

$$\rho = 1 - \alpha \quad (36)$$

Note that the exchange factor, \mathcal{F}_{12} , is different from the view factor, F_{12} in Eqn. (11), since the exchange factor has the radiative properties of the materials wrapped up in the definition, while the view factor is purely geometric.

Now there are two nonlinear equations with unknowns T_1 and T_2 . These equations can be solved via Newton's

method for a system of equations, where the residual equations are

$$\left. \begin{aligned} R_1 &= 4\pi k_1 \frac{r_1 r_i}{r_1 - r_i} (T_i - T_1) - A_1 \mathcal{F}_{12} \sigma (T_1^4 - T_2^4) = 0 \\ R_2 &= 4\pi k_2 \frac{r_2 r_o}{r_o - r_2} (T_2 - T_o) - A_1 \mathcal{F}_{12} \sigma (T_1^4 - T_2^4) = 0 \end{aligned} \right\} \quad (37)$$

and the Newton update equation is

$$\begin{bmatrix} \frac{\partial R_1}{\partial T_1} & \frac{\partial R_1}{\partial T_2} \\ \frac{\partial R_2}{\partial T_1} & \frac{\partial R_2}{\partial T_2} \end{bmatrix}^{\nu} \begin{bmatrix} \Delta T_1 \\ \Delta T_2 \end{bmatrix}^{\nu+1} = - \begin{bmatrix} R_1 \\ R_2 \end{bmatrix}^{\nu} \quad (38)$$

where ν denotes the iteration level. The Jacobian terms are given by

$$\frac{\partial R_1}{\partial T_1} = -4\pi k_1 \left(\frac{r_1 r_i}{r_1 - r_i} \right) - 4A_1 \mathcal{F}_{12} \sigma T_1^3 \quad (39)$$

$$\frac{\partial R_1}{\partial T_2} = 4A_1 \mathcal{F}_{12} \sigma T_2^3 \quad (40)$$

$$\frac{\partial R_2}{\partial T_1} = -4A_1 \mathcal{F}_{12} \sigma T_1^3 \quad (41)$$

$$\frac{\partial R_2}{\partial T_2} = 4\pi k_2 \left(\frac{r_2 r_o}{r_o - r_2} \right) + 4A_1 \mathcal{F}_{12} \sigma T_2^3 \quad (42)$$

The exact solution for the radiation exchanging surface temperatures are

$$T_1 = 578.22506 \text{ K and } T_2 = 1035.0238 \text{ K} \quad (43)$$

and the surface heat fluxes are given by

$$\dot{q}_1 = 27822.506 \text{ W/m}^2 \text{ and } \dot{q}_2 = -12365.558 \text{ W/m}^2 \quad (44)$$

3. Grid Refinement Study

Since the intent of the problem is to determine the order of accuracy of the approximate enclosure radiation method, deviation from the standard grid refinement methodology used in the previous sections is necessary. In order to isolate the errors caused by the enclosure radiation boundary condition, it is necessary to account for the errors contributed by the discretized conduction term which has previously been verified to be second order accurate. Instead of the error metric for the enclosure radiation problem being the error between the numeric and analytic solutions, the approach will be as follows:

1. For each grid refinement level, solve the concentric spherical shell problem with specified heat flux conditions

on the outer surface of the inner shell and the inner surface of the outer shell given the exact heat fluxes in Eqn. (44). The boundary conditions for this problem are

$$T(r = r_i) = T_i$$

$$\dot{q}(r = r_1) = \dot{q}_1$$

$$\dot{q}(r = r_2) = \dot{q}_2$$

$$T(r = r_o) = T_o$$

These solutions represent the numerical result on each grid level if the enclosure radiation terms were exact.

2. For each grid refinement level, solve the concentric spherical shell radiation gap problem.
3. For each grid refinement level, calculate the error between the solutions in steps 1 and 2, and determine the order of accuracy of the enclosure radiation boundary condition.

A series of three successively refined hexahedron meshes were use in this study and are outlined in Table 2. Since it is not the intent to observe the error in the conduction term as the grid is refined, the grid refinement was only performed in angular directions while keeping the radial element distribution constant between grid levels. Inner and outer views of a hemisphere of the fine mesh can be seen in Figure 2. Since no independent steady-state option is implemented in *CHAR*, transient solutions were run until the temperature field no longer changed.

The grid convergence results can be seen in Figure 3. Unlike previous problems, the error metrics for this problem were chosen to be the RMS error in temperature of the radiating faces with a reference value of $Q_o = T_i = 300$ K in Eqn. (??). The grid metric (Number of Elements in One Dimension) was chosen to be the square root of the number of nodes on each of the radiating faces, which varied by a factor of two between grid levels. It was unknown what the convergence rate of the view factor methodology would be a priori, but it was not necessarily expected to be a smooth trend based on the assumptions of the methodology. Figure 3 shows the convergence rate for the temperatures on the radiating surfaces. While the correct answer is approached as the mesh is refined, it is not clearly evident what the convergence rate is. Perhaps there is a more appropriate error metric or grid refinement methodology to manifest the order of accuracy, but the results from this study instill confidence that the methodology is correctly implemented.

Table 2. Hexahedron mesh parameters for spherical shell radiation gap problem.

Grid Name	N	N_e
Coarse	1764	1536
Medium	6948	6144
Fine	27,684	24,576

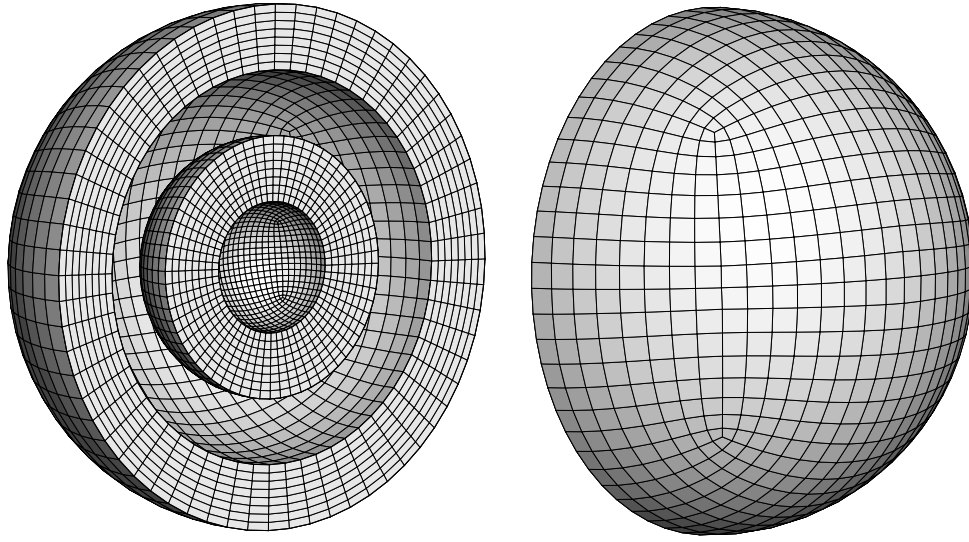


Figure 2. Concentric spherical shells fine mesh.

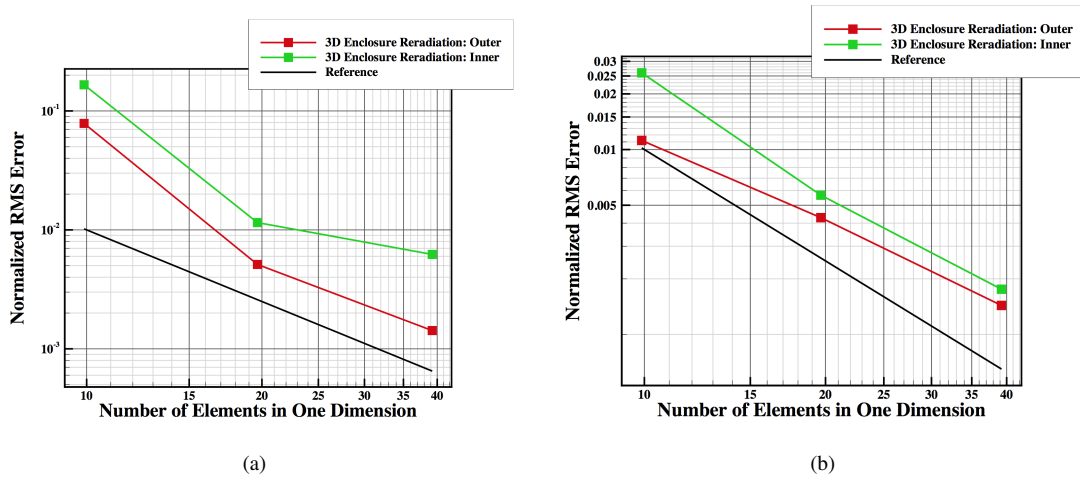


Figure 3. Grid convergence results for enclosure reradiation verification problem using (a) double area integral method and (b) monte carlo method.

B. Code-to-Code 3D Cavity Problem

One of the main motivations to implement some of the enclosure radiation capabilities within *CHAR* was the design of the cavity heating tiles experiment on Orion's EFT-1 mission. The cavity heating tiles were two tiles on the vehicle's backshell, each with a cylindrical cavity cut-out on the surface of the tile to mimic damage due to an MMOD impact. These cavities were designed with 1" diameters, and with depths of 1" and 1.4" [3]. Figure 4 shows the two cavity

tiles installed on the Orion backshell before the EFT-1 mission. During design of these cavities, *CHAR* was used to analyze the thermal response of these tiles, which required many enclosure reradiation calculations. In these features, the fraction of heating to the tile due to energy being absorbed, emitted and reflected within the cavity walls is non-negligible and must be accounted for. To instill confidence in *CHAR*'s ability to correctly model this problem, a preliminary code-to-code comparison was carried out against the commercial software SINDA/FLUINT 5.6 Patch Level 9 [2], which has been heavily used in the past within NASA for tile thermal analysis. For this problem SINDA was used through the Thermal Desktop (TD) interface, and radiation calculations were performed using the RadCAD module available within SINDA.

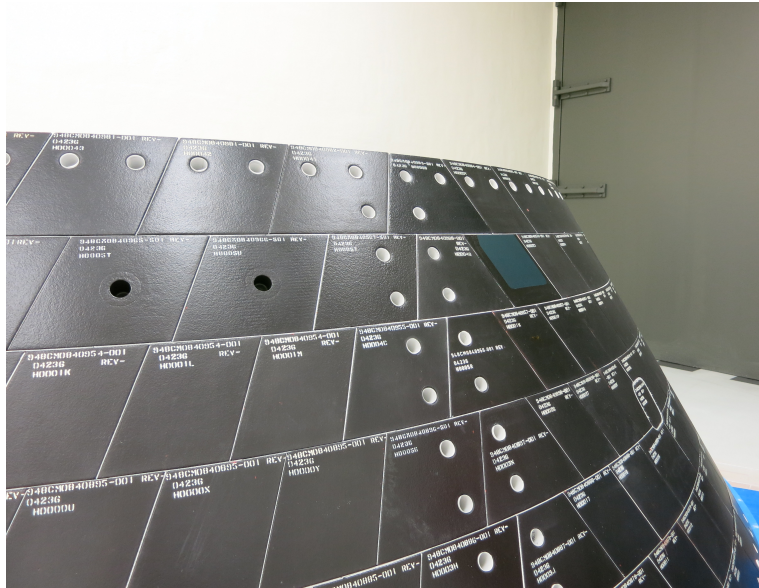


Figure 4. Orion EFT-1 cavity heating tiles. [3]

The problem was modeled individually by two different designers, each using his own best practices for the thermal software being run. The problem involved a realistic time- and space- dependent aeroheating boundary condition on a half-symmetry domain of the 1.4"-deep cavity tile, which was allowed to reradiate to a constant far-field temperature. The sidewalls of the domain, including the symmetry plane were modeled as adiabatic, and the (inner) backwall of the tile structure was also set as adiabatic. On the inner cavity surfaces, in addition to the specified heating distribution within the cavity, an enclosure reradiation boundary condition was set, with any view factor to space reradiating to a constant sink temperature.

Despite several attempts to import the finite element mesh created for the *CHAR* analysis into Thermal Desktop, the number of elements in this grid (315,000) was too many to comfortably handle in Thermal Desktop. Therefore, a separate mesh was developed for the SINDA/TD analysis which consisted of 30,000 nodes. Both grids employed tighter element clustering near the surface of the tile and the cavity walls, tight clustering underneath the cavity floor, while keeping the surface elements on the cavity enclosure as large as possible to ensure convergence when computing

radiation view factors. The gridded geometry included the tile, reaction cured glass coating (RCG) on the surface of the tile, and several substructure layers. Both, the *CHAR* and SINDA grids used for this analysis are shown in Figure 5.

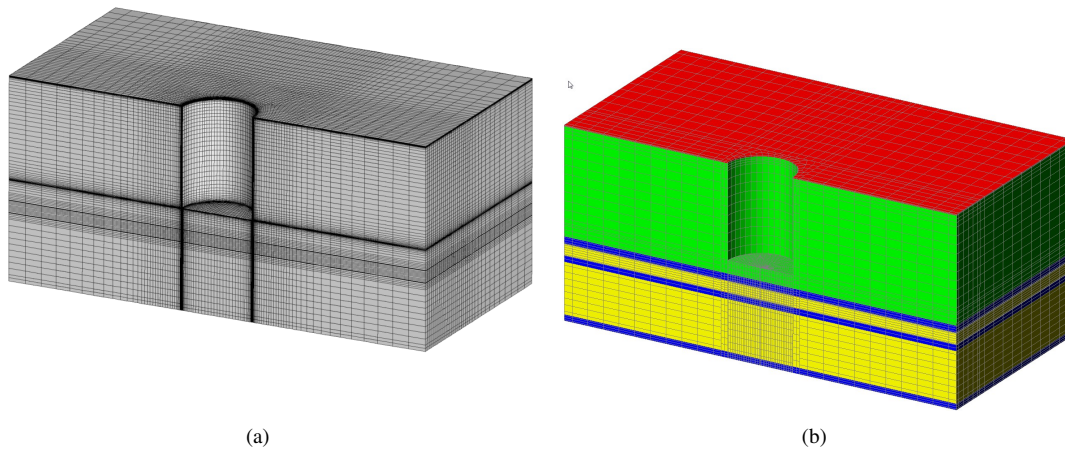


Figure 5. Grids used for code-to-code cavity problem for (a) *CHAR* simulations and (b) TD/SINDA simulations.

A monte carlo ray tracing approach was used with both solvers to compute geometric view factors. For the SINDA model, 5 million rays were cast per node to achieve convergence, while the *CHAR* results for this problem were converged after shooting 1 million rays per element. Also, to closely mimic the numerics in SINDA/TD, *CHAR* was run assuming a trapezoidal integration rule and linear pressure interpolation in conductivity table lookups.

Comparisons were made at the ten different locations shown in Figure 6 and the comparisons between the two codes are presented in Figure 7. Considering differences in grids and the numerics of each code, the results at all ten locations show excellent agreement between the two solvers. Even though further work could isolate grid and numerics differences in this comparison, the close agreement between the two codes serves as additional evidence to verify the implementation of the enclosure reradiation boundary condition in *CHAR*.

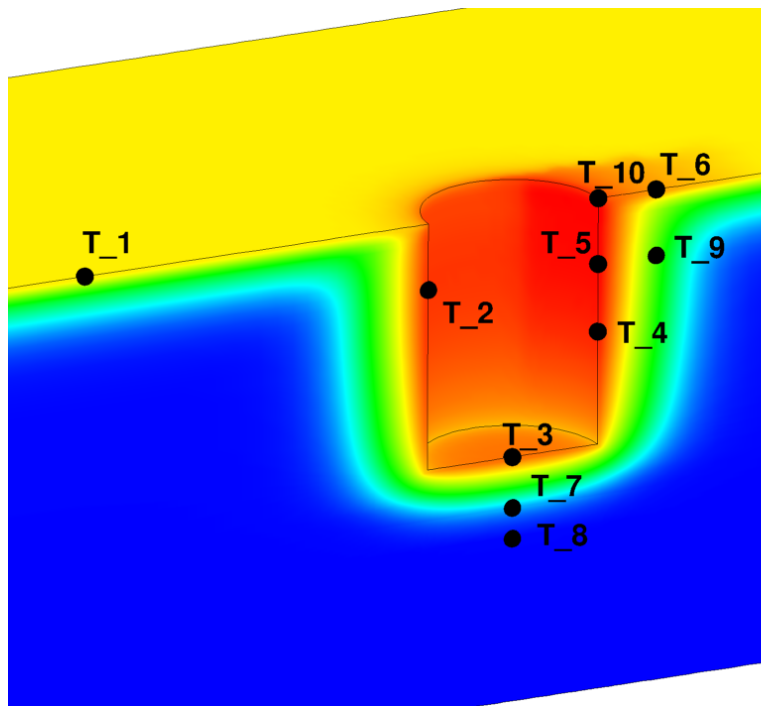


Figure 6. CHAR vs. SINDA/RADCAD comparison locations.

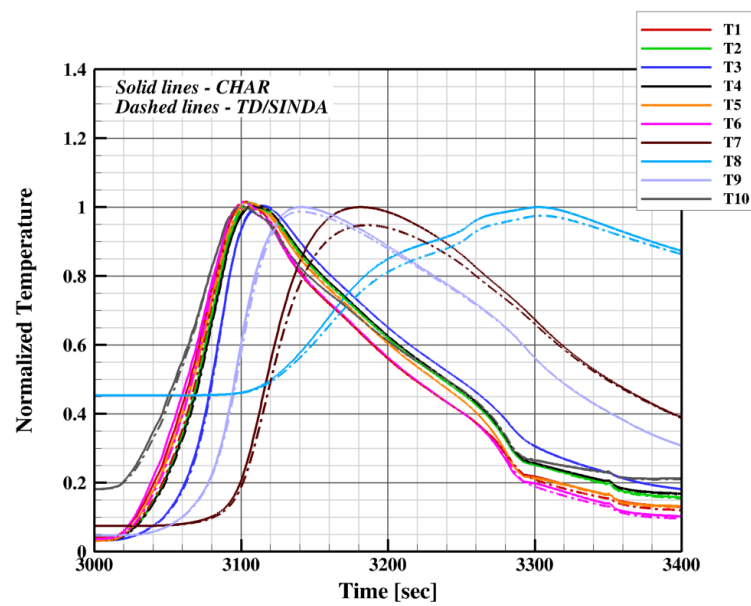


Figure 7. CHAR vs. SINDA/RADCAD comparison results.

IV. EFT-1 Radiant Tile Experiment

As part of a calibration effort of Orion EFT-1 flight thermocouples, a small radiant test fixture was developed in house at NASA JSC. The fixture consists of a simple aluminum stand which supports an instrumented susceptor plate (or "hot plate"), which is heated by a 500W ceramic IR heater. Figure 8 presents a graphical representation of the operation of the radiant test rig, as well as a photo of the actual assembly. A second small aluminum frame with threaded feet is used to place the test article, in this case instrumented AETB8 flight tiles, as close as possible to the hot plate without making contact. By using the threaded feet to adjust the test article's position, the distance between the hot plate and the test article surface can be adjusted to the desired specification. The hot plate is insulated from the support structure as much as possible by using FRCI-12 ceramic insulation tiles to obtain uniform thermal conditions on the hot plate to improve calibration accuracy. Additionally, the hot plate is instrumented on the side exposed to the test article with a Type-E foil thermocouple and bonded using high temperature RTV. At the time of this experiment, the RTV temperature limits set the operating temperature limit for the radiant rig at approximately 625°F, however, additional improvements are being planned in order to allow higher operating temperatures. Obtaining a measurement on this hot plate was of utmost importance in the calibration of these thermocouples, since that temperature history can be directly used as a boundary condition in the thermal model.

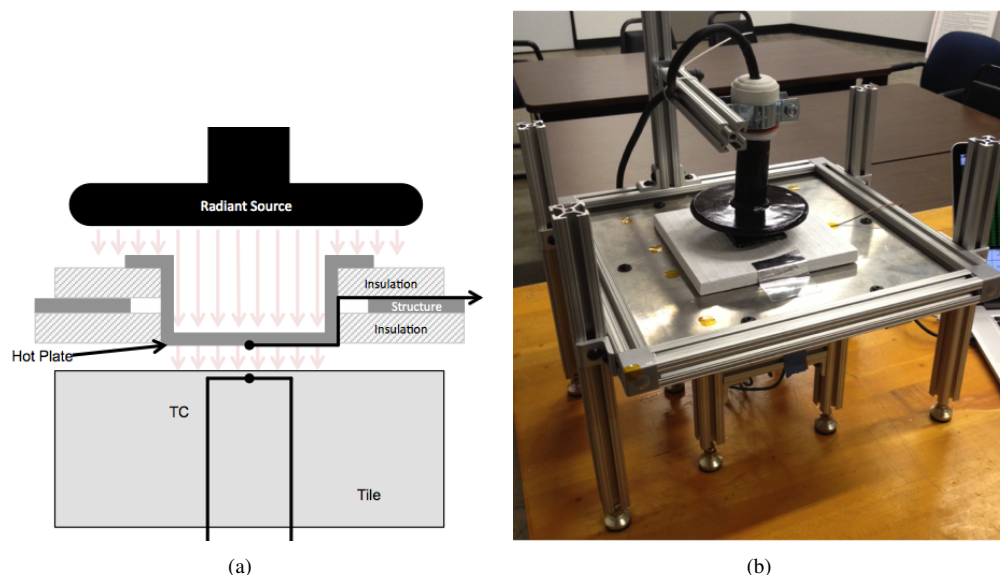


Figure 8. Radiant test rig configuration .

The real objective of the calibration test was to obtain data on non-standard thermocouple installations on the EFT-1 cavity heating tiles. However, the details of that instrumentation and calibration are left out of this work for the sake of brevity. Additional details can be found in ([Paper to be published in ITAR session in this conference](#)). The work and data described here focuses on data obtained on a flight tile with nominal thermocouple installations. This type of installation results in minimal thermal lag and minimizes thermal losses down the lead wires of the

TC, and therefore the recorded temperature very closely describes the actual surface temperature. Furthermore, these "nominal" thermocouple installations have a great deal of flight heritage, as they closely follow the tile instrumentation used in the Space Shuttle program.

Testing was carried out in a large vacuum chamber at the Lockheed Martin Materials Testing Lab in Denver, Colorado. This facility allowed for testing at very low pressures (1×10^{-3} Pa), thereby allowing the thermal model to neglect any effects due to natural convection. The facility's data acquisition system was set up to record temperatures from the flight instrumentation, from the hot plate, thermocouples located on the back (cool) side of the tile, and many other instruments located on the test stand and on a surrounding shroud. The set-up of the radiant test fixture inside of the vacuum chamber, with a tile test article underneath is presented in Figure 9.

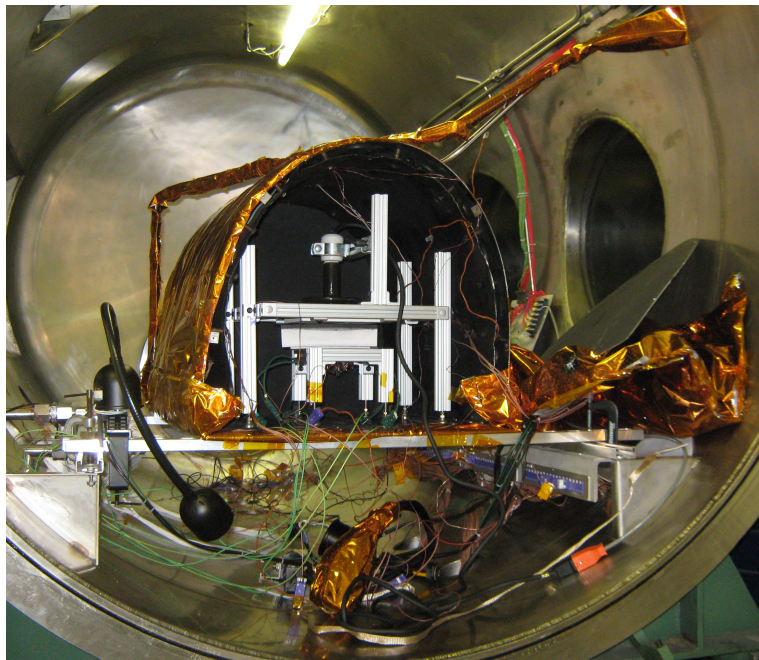


Figure 9. Radiant test set up in vacuum chamber.

The focus of the present effort is modeling the calibration experiment in *CHAR* driving the model using test conditions from test run 7, which targeted a surface temperature of 550K. Figure 10 illustrates the location of the six surface thermocouples on the test tile, however, given the 2"x2.4" area of the hot plate, the hot plate was centered around TCs 1-4. Modeling the response at TCs 5 and 6 was not attempted in this work due since they lied well outside of the hot plate and surrounding insulation region. The data collected from the four relevant sensors, as well as the hot plate and the chamber pressure, are presented in Figure 11.

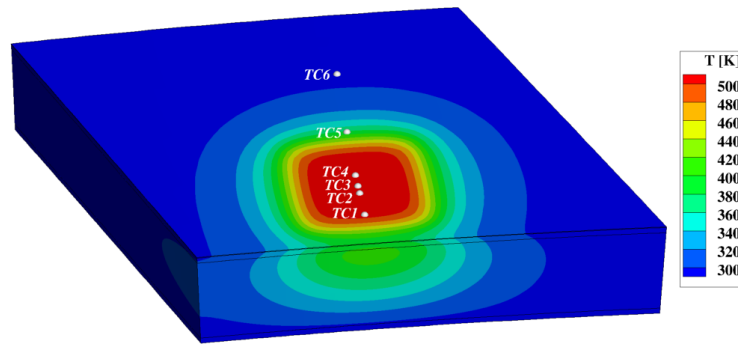


Figure 10. Temperature contours and TC locations of radiant test tile.

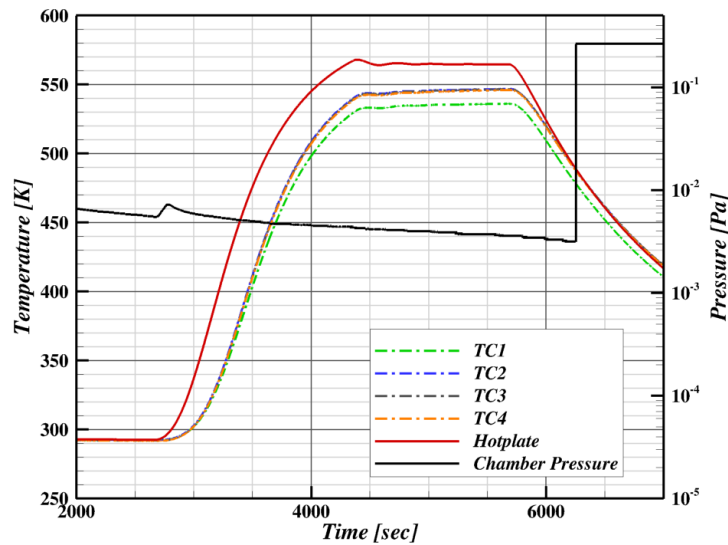


Figure 11. Radiant test data.

The thermal model grid was developed from the flight tile CAD in order to capture the tile's curvature and exact shape. The mesh was developed using the Hypermesh gridding package from Altair's Hyperworks tools. It consisted of 147,000 prismatic and hexahedral elements which included the tile test article as well as the hot plate and the surrounding insulation. A preliminary grid convergence study showed this grid density to be adequate for modeling of the calibration experiments, and with few enough surface elements participating in the radiation exchange for a

practical solution of this problem. An illustration of the grid used in this study is shown in Figure 12.

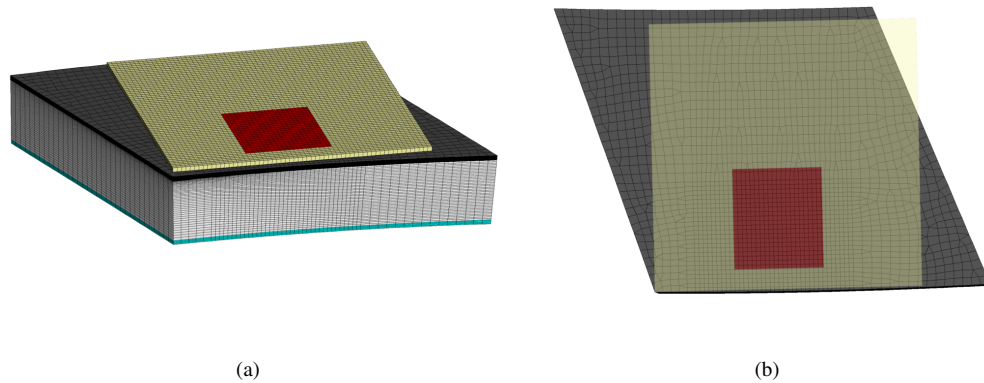


Figure 12. Grid used in CHAR thermal analysis of radiant test.

The hot plate temperature recorded during the experiment was applied as a fixed temperature boundary condition to the outer surface of the hot plate in the thermal model, while the inner surfaces participated only in an enclosure radiation exchange. Temperature and pressure dependent material properties were used for the tile domains, while a constant emissivity (measured at room temperature before testing) was assumed for the hot plate. The hot plate was modeled as aluminum with a fictitious high conductivity in order to maintain a uniform temperature across the hot plate. The results of this modeling effort are compared with the test data in Figure 13. These results show excellent agreement with the calibration data, with differences less than 3K for TCs 2,3 and 4. Slightly larger differences of 6K are seen for TC 1, however, the close proximity of this TC to the edge of the tile domain during these long test times introduces additional uncertainty related to the appropriate boundary condition to apply on the tile sidewall near TC 1. In the end, the ability to correctly model this purely radiant experiment using the enclosure radiation capabilities within *CHAR* provides initial validation of the software.

Ongoing and Future work

Future work will continue development of the reflection algorithm within *CHAR*, and explore if there are any other ways to handle internal reflections which could result in code speedup. In addition, the ability to recompute view factors as the mesh moves will be added to the code, and a sample ablating cavity problem will be presented.

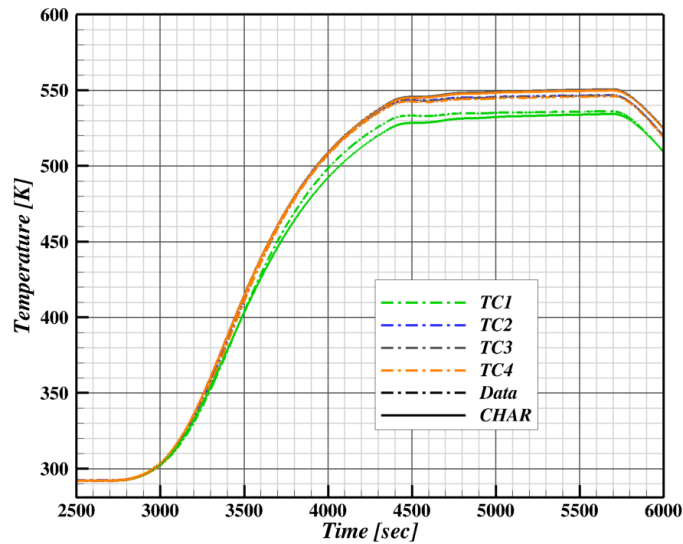


Figure 13. Radiant test modeling results.

References

- [1] Balay, S., Buschelman, K., Eijkhout, V., Gropp, W. D., Kaushik, D., Knepley, M. G., McInnes, L. C., Smith, B. F., and Zhang, H., "PETSc Users Manual," Tech. Rep. ANL-95/11 - Revision 2.3.0, Argonne National Laboratory, April 2004.
- [2] "Sinda/Fluint, General Purpose Thermal/Fluid Analyzer, User's Manual," April 2013.
- [3] Kremer, K., "Heat Protecting Back Shell Tiles Installed on NASA's Orion EFT-1 Spacecraft Set for Dec. 2014 Launch," <http://www.universetoday.com/114064/heat-protecting-back-shell-tiles-installed-on-nasas-orion-eft-1-spacecraft-set-for-dec-2014-launch/>, August 2014, [Online; posted 30-August-2014].